Effective heating of nonadiabatic protons in magnetic reconnection with a guide field

Effective heating of nonadiabatic protons in magnetic reconnection with a guide field

Shunsuke Usami[*]

Department of Helical Plasma Research,

National Institute for Fusion Science,

National Institutes of Natural Sciences, Toki 509-5292, Japan.

Ritoku Horiuchi and Hiroaki Ohtani

Department of Helical Plasma Research,

National Institute for Fusion Science,

National Institutes of Natural Sciences, Toki 509-5292, Japan.

SOKENDAI (The Graduate University for Advanced Studies), Toki 509-5292, Japan.

(Dated: July 21, 2017)

Abstract

Mechanism of plasma heating through magnetic reconnection with a guide magnetic field is investigated by means of two-dimensional electromagnetic particle simulations. These simulations mimic dynamics of two torus plasmas merging through magnetic reconnection in a spherical tokamak (ST) device. It is found that a large part of protons, which behave as nonadiabatic, are effectively heated in the downstream, because a ring-like structure of proton velocity distribution is observed at a local point in the downstream. The characteristic features of the velocity distribution can be explained as the following proton motion. Upon entering the downstream across the separatrix, nonadiabatic protons suddenly feel the strong electromagnetic field in the downstream and move in the outflow direction while rotating mainly around the guide magnetic field. The protons gain kinetic energy not only on the separatrix but also in the downstream. This effective heating process can be interpreted as the "pickup," which, however, was thought to be responsible for only heavy ions. In this work, it is demonstrated that the pickup of protons is compatible with the known pickup theory in the cases in which the plasma beta is much less than 1, which is satisfied in STs.

PACS numbers: 52.65.-y, 52.35.Vd, 52.65.Rr, 52.55.Fa

---

*Electronic address: usami.shunsuke@nifs.ac.jp

I. INTRODUCTION

The spherical tokamak (ST) attracts attention as a candidate for future fusion reactors, because STs enable the confinement of a higher-beta plasma compared with standard tokamaks [1]. In plasma merging experiments of STs, two torus plasmas are merged together to form a single torus plasma under magnetic compression. At the contact point of the initial two torus plasmas magnetic reconnection occurs, and a single torus plasma with high temperature is formed [2, 3].

In plasma merging experiments it is observed that electrons are heated significantly in the vicinity of the contact point, namely, the reconnection point, whereas ions are heated mainly in the downstream of reconnection [2–4]. The mechanism of such plasma heating is considered to be crucial for a complete understanding of high-beta plasma formation. Clarification of the heating mechanism and control of heating may lead to higher-performance of STs for realizing economical ST reactors in the future. In past works, as the ion heating mechanism, for example, shock or viscosity heating [4], thermalization via remagnetization, collisions, and scattering by wave-particle interactions [5], and phase mixing due to the finite Larmor radius effect inside secondary magnetic islands [6, 7] have been suggested. In this paper, we report the simple heating mechanism for nonadiabatic ions (protons).

The paper is organized as follows. In Sec. II, we explain our particle simulation model for collisionless driven reconnection in an open system. We demonstrate that ions are effectively heated in the downstream and analyze nonadiabatic ion motions in Sec. III. In Sec. IV, we discuss relations between the heating process and the known "pickup" theory. Section V provides a summary of this work.

II. SIMULATION METHOD

We investigate the ion heating mechanism in the downstream by means of two dimensional electromagnetic particle-in-cell (PIC) simulations. Microscopic kinetic effects originating from stochastic particle motions play essential roles in the energy transfer process [8]. Figure 1 shows the schematic diagram of our simulation model. The two torus plasmas in an ST device are depicted in the left part, and the area simulated by our PIC code "PASMO" [9, 10] is depicted in the right part. This PIC area covers the kinetic region including the

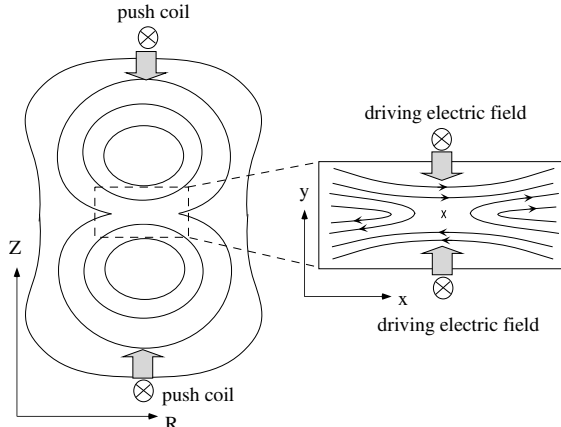central reconnection point, and thus can mimic the region near the contact point of merging plasmas [11].

FIG. 1: Schematic diagram of plasma merging experiments in a spherical tokamak device. The dotted boxed area covering the kinetic region including the contact point is calculated by our particle simulation code "PASMO."

The initial condition is one-dimensional equilibrium with an antiparallel magnetic field in the x direction and a uniform guide magnetic field in the z direction, that is, $B_x(y) = B_{x0}\tanh(y/L)$ and $B_z(y) = B_{z0}$ for the magnetic field, and $P(y) = P_0 + B_{x0}^2/(8\pi)\text{sech}^2(y/L)$ for the plasma pressure, where B_{x0}, B_{z0}, and P_0 are constants and L is the spatial scale. The initial particle velocity distribution is a shifted Maxwellian distribution with the averaged velocity equal to the diamagnetic drift velocity. The temperature is uniform and the ion-to-electron temperature ratio is taken to be $T_{i0}/T_{e0} = 1.0$. The simulation parameters are as follows. The ion-to-electron mass ratio is $m_i/m_e = 100$, and the ratio of the electron plasma frequency to the electron gyrofrequency is $\omega_{pe}/\omega_{ce} = 6.0$. Here, we define that $\omega_{ce} = eB_{x0}/m_e c$, where c is the speed of light. The simulation domain size is $2x_b \times 2y_b = 10.54(c/\omega_{pi}) \times 2.63(c/\omega_{pi})$, where ω_{pi} is the ion plasma frequency. The time step is $\omega_{pi}\Delta t = 0.0052$. The grid spacing is $\Delta_g/(c/\omega_{pi}) = 0.010$. The initial total number of particles is 14,090,240.

An open boundary condition is implemented in PASMO [12]. At the upstream boundary ($y = \pm y_b$), in order to generate plasma inflows, an external driving electric field E_d is imposed in the direction perpendicular to the magnetic field. In this paper, perpendicular and parallel indicate perpendicular and parallel to the local magnetic field at each position, respectively.

4

(In some explanations below, the uniform magnetic field is supposed.) The driving field E_d supplies particles which satisfy the shifted Maxwellian velocity distribution and flow into the simulation domain from the upstream boundary with the $E \times B$ drift velocity. The field E_d, which is set to zero at the initial time, begins to grow first near the center of the upstream boundary ($x = 0, y = \pm y_b$), and develops so as to reach $E_{dz} = -0.04 B_{x0}$, where E_{dz} is the z-component of E_d. On the other hand, the downstream boundary ($x = \pm x_b$) is free, and particles can freely go in and out through the downstream boundary.

III. RESULTS

A. Ring-like structure formation of velocity distribution

We performed a particle simulation in the case of $B_{z0}/B_{x0} = 2.0$, $L/(c/\omega_{pi}) = 0.66$, and $P_0/(B_{x0}^2/8\pi) = 0.35$. The Alfvén speed is $v_A = 0.037c$ for the magnetic field $B_0 = \sqrt{B_{x0}^2 + B_{z0}^2}$ and the plasma density at the neutral sheet. In Fig. 2, we show simulation results at $\omega_{ce}t = 1292$, where the electromagnetic field, the velocity, and the temperature are normalized to B_{x0}, c, and $m_e c^2$, respectively. Figure 2(a) displays the spatial profile of the out-of-plane component of the magnetic field B_z (the color contours) and the magnetic field lines. Magnetic reconnection is driven by plasma inflows supplied from the upstream and the reconnection point lies almost at the center. The reconnection electric field is balanced with the driving electric field at the upstream boundary [10, 13], and the reconnection system is in a quasi-steady state. The out-of-plane component of the magnetic field is composed of the initial uniform B_{z0} and the quadrupole structure produced by the Hall current, as is well known. In addition, the magnetic separatrix is clearly seen. Figure 2(b) illustrates the vectors of the ion bulk velocity $\boldsymbol{u}_i$ (the arrows) and the y-component of the electric field E_y (the color contours). We can see that E_y, which is dominantly the convective electric field, is produced in almost the entire downstream. The velocity vectors show that bipolar outflows emanate from the reconnection point. The ions moving from the upstream into the downstream are classified into two groups. One group is ions entering the downstream through the reconnection point, and the other group is ions moving across the separatrix, which can be effectively heated. We plot the dotted line as a streamline of averaged ion motions, along which an element of the ion fluid moves from the upstream to the downstream.

In this work, we mainly consider ion behaviors along the streamline from the upstream to the immediate downstream $[1.0 \lesssim x/(c/\omega_{pi}) \lesssim 4.0]$. In contrast, the dynamics in the deep downstream are not discussed. In Fig. 2(c), we show the ion temperature perpendicular to the magnetic field $T_{i\perp}$, which rises in the downstream, as shown experimentally. The ion temperature in the vicinity of the reconnection point also increases. However, the increase comes from the characteristics of the ion meandering motion [14]. This process is not discussed in this paper.
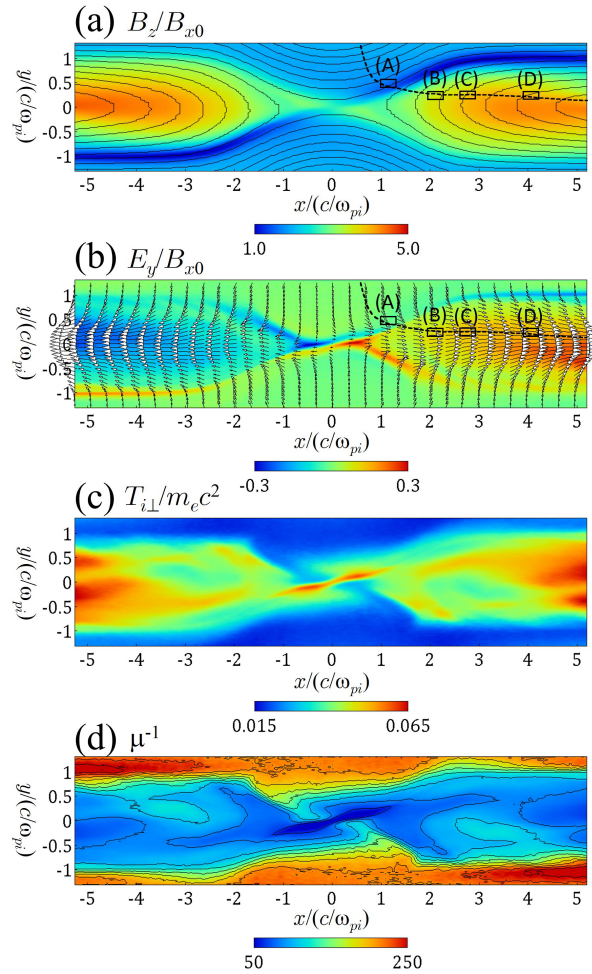

FIG. 2: Spatial profiles of (a) magnetic field lines and B_z, (b) ion bulk velocity vectors and E_y, (c) ion temperature perpendicular to the magnetic field, and (d) average of inversed ion magnetic moments. The electromagnetic field, the velocity, and the temperature are normalized to B_{x0}, c, and $m_e c^2$, respectively.

In order to investigate the ion heating mechanism in the downstream, we examine the

change in ion velocity distributions at several local points along the streamline. In Figs. 3(a)-(d), we show the ion velocity distributions integrated over the boxed areas (A)-(D) designated in Fig. 2, respectively. The boxed areas (A)-(D) are located (A) on the separatrix, (B) and (C) in the immediate downstream, and (D) in the deep downstream, respectively. Figure 3(a) indicates that most ions have negative v_y to enter the downstream. The initial shifted-Maxwellian distribution of ions is nearly maintained without being effectively heated significantly. In contrast, Figs. 3 (b) and (c) demonstrate that the distributions spread mainly in the v_x direction and ring-like structures are formed. That is, ions are effectively heated in the immediate downstream. Here, note that not only selected ions are displayed, but all the ions in the boxed area are displayed. We can see that a large part of the ions are associated with the formation of the ring-like structure. The effective thermal velocities are calculated to be approximately $0.022c$ both for Figs. 3 (b) and (c). Further out in the downstream, it seems that the ring-like structure begins to collapse as shown in Fig. 3(d).

Further analyzing the ring-like structure in the velocity distribution of Fig. 3(c), it is found that the center of the circle (ring) is located at $(v_x, v_y) \simeq (0.03, 0.0)c$ and its radius is nearly equal to $0.03c$. On the other hand, the outflow speed is observed to be approximately $0.03c$ at the boxed area (C). That is, the ring-like structure has the characteristic features that the radius and the distance between the center and the origin are equal to the outflow speed. Here, note that the center position and the radius in the velocity space are measured directly from the view of Fig.3(c). The radius of the velocity circle ($0.03c$) does not completely correspond to the effective thermal velocity ($0.022c$) obtained by assembling ion particle velocities statistically. This is because in the velocity space, ions are not uniformly distributed on the ring. If the ion distribution were uniform on the ring, the radius would be equal to the effective thermal velocity. This result will perform an essential role in considering what component of the electric field energizes ions. This issue will be discussed below.

The characteristic features of the velocity distribution can be explained as follows. The periods of time during which some ions pass across the separatrix are comparable to or shorter than their gyroperiods. In order to comprehend the behaviors of such ions, we can not employ the guiding center drift. However, we must take into account the orbits of individual ions. Now, we define such particles as behaving as "nonadiabatic." When the nonadiabatic ions enter the downstream across the separatrix, they suddenly feel the strong

7

electromagnetic field, which mainly consists of B_z, the out-of-plane magnetic field and $E_\perp$, the electric field perpendicular to B_z. Their entry speed can be regarded as much smaller than the outflow speed in the downstream. The nonadiabatic ions rotate around B_z moving in the x direction owing to the $E \times B$ drift. From Fig. 2(d), in which the averaged value of the inversed ion magnetic moment $\mu^{-1} = B/(m_i \langle v_{i\perp} - \langle v_{i\perp} \rangle \rangle^2/2) = B/T_{i\perp}$ is displayed, we can see that μ sharply increases near the separatrix. Here, $v_{i\perp}$ is the ion particle velocity perpendicular to the magnetic field and $\langle \rangle$ denotes the ensemble average. The behaviors of some ions at least are nonadiabatic when they cross the separatrix.
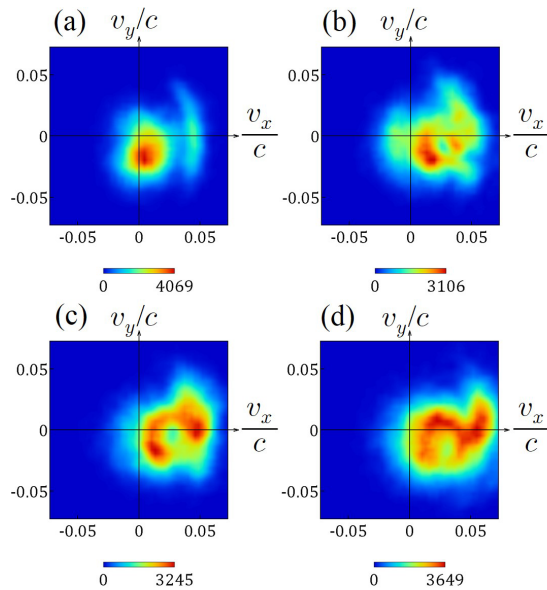

FIG. 3: Ion velocity distributions at the local regions (A)-(D) of Fig. 1. The panels (b) and (c) show ring-like structures.

In order to understand ion behaviors better, we explain the orbits of nonadiabatic ion particles in the downstream. In order to avoid complicated explanations, let us consider the ion orbits in the following simplified geometry in the downstream, namely, the outflow u_out [1], the perpendicular electric field $E_\perp$, and the magnetic field B are taken to be in the $\tilde{x}$, $\tilde{y}$, and $\tilde{z}$ directions, respectively. Here, we ignore the presence of the electrostatic field and the electric field parallel to the magnetic field, which are confirmed to be negligibly-small compared with

---

[1] *In the strict sense, the outflow is allowed to have the component parallel to the magnetic field. However, we suppose that u_out has only the perpendicular component, which produces the convective electric field in the $\tilde{y}$ direction $\boldsymbol{E}_\perp = -\boldsymbol{u}_\text{out} \times \boldsymbol{B}$.*

$E_\perp$. Transforming the coordinate system to the frame moving in the $\tilde{x}$ direction with the velocity $u_{\rm out}$, in which the downstream plasma does not move, nonadiabatic ions enter the downstream with the velocity $\boldsymbol{v} \sim (-u_{\rm out}, 0, 0)$ across the separatrix, assuming that $v_{\tilde{y}}$ and $v_{\tilde{z}}$ are much smaller than $u_{\rm out}$. In this moving frame, the electromagnetic field in the downstream is expressed as $\boldsymbol{E} \sim (0, 0, 0)$ and $\boldsymbol{B} \sim (0, 0, B_{\tilde{z}})$. In this electromagnetic field, the ions rotate with the speed $u_{\rm out}$ around $B_{\tilde{z}}$, and this is the simple gyromotion in the $(\tilde{x}, \tilde{y})$ plane. Now let us return to the original frame and observe this ion motion. In the original frame, the ions rotate with the speed $u_{\rm out}$ moving in the $\tilde{x}$ direction with the averaged velocity $u_{\rm out}$. This trajectory is cycloid due to the $E_\perp \times B$ drift motion.
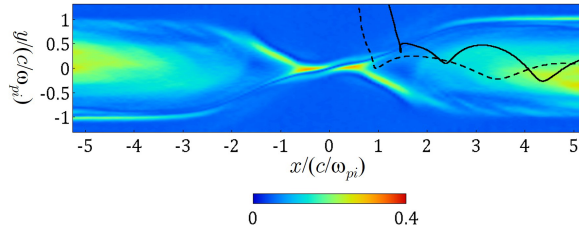

FIG. 4: Trajectories of nonadiabatic ions calculated in the electromagnetic field given in Fig. 2. The color contours indicate the strength of $E_\perp$ normalized to B_{x0}.

In order to observe the orbits of nonadiabatic ions effectively heated, we perform test particle simulations by using the electromagnetic field given in Fig. 2. We plot two typical orbits of test ion particles in Fig. 4. The color contours indicate the perpendicular electric field $E_\perp$. Here, it should be kept in mind that unlike the simplified geometry, $E_\perp$ has not only the dominant y-component but also the x- and z-components. Initially, the test ions are placed on the upper upstream boundary. Their initial velocities are taken to be equal to the ion bulk velocities at the initial positions. The solid line indicates the ion orbit with the initial position $(x, y) = (1.2, 1.3)c/\omega_{pi}$ and the initial velocity $(v_x, v_y) = (0.0052, -0.013)c$. The dotted line denotes the orbit for the case of the initial position $(x, y) = (0.60, 1.3)c/\omega_{pi}$ and the initial velocity $(v_x, v_y) = (0.0019, -0.012)c$. We can see that both of the two ions move in the x direction with the gyromotion, and these trajectories are cycloid-like curves. The ring-like structure in the velocity distribution is formed by such ions.
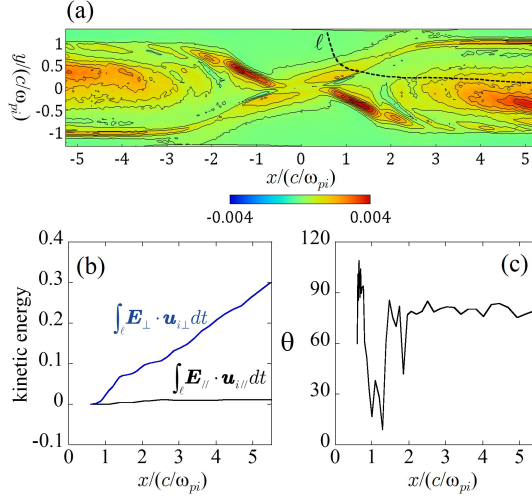
9

FIG. 5: (a) Profiles of $\boldsymbol{E} \cdot \boldsymbol{u}_i$, (b) the integral of the perpendicular (the blue line) and parallel (the black line) components of $\boldsymbol{E} \cdot \boldsymbol{u}_i$, and (c) the angle between $\boldsymbol{E}_\perp$ and $\boldsymbol{u}_{i\perp}$ along the streamline ℓ [the dotted line of the panel (a)]. Ions gain kinetic energy from $\boldsymbol{E}_\perp$ not only on the separatrix but also in the downstream. It is of interest that $\boldsymbol{u}_{i\perp}$ is nearly parallel to $\boldsymbol{E}_\perp$ on the separatrix and is nearly perpendicular to $\boldsymbol{E}_\perp$ in the downstream. The electric field, the velocity, and the time are normalized to B_{x0}, c, and ω_{pi}^{-1}, respectively.

B. Gain of kinetic energy

Furthermore, we investigate where and by what components of the electric field the ions gain kinetic energy through the effective heating process described above. In Fig. 5(a), we show the inner product of $\boldsymbol{E}$ and $\boldsymbol{u}_i$ which is normalized to $B_{x0}c$. Ions gain energy not only on the separatrix but also in the downstream. Ion behaviors are analyzed along the streamline represented as the dotted line. In Fig. 5 (b), we plot $\int_\ell \boldsymbol{E}_\perp \cdot \boldsymbol{u}_{i\perp} dt$ (the blue line) and $\int_\ell \boldsymbol{E}_\parallel \cdot \boldsymbol{u}_{i\parallel} dt$ (the black line), which mean the perpendicular and parallel components of the integral of $\boldsymbol{E} \cdot \boldsymbol{u}$ along the streamline ℓ. We can clearly see that ions gain kinetic energy dominantly from the perpendicular electric field. At first glance, it seems startling that the $E_\perp \times B$ drifting particle gains energy from $E_\perp$. In order to solve this apparent inconsistency, we plot the angle θ between $\boldsymbol{E}_\perp$ and $\boldsymbol{u}_{i\perp}$ along ℓ in Fig. 5 (c). On the separatrix $[x/(c/\omega_{pi}) \simeq 1.0]$, the ion bulk velocity $\boldsymbol{u}_{i\perp}$ is nearly parallel to $\boldsymbol{E}_\perp$, which is dominated by the electrostatic field [8, 13]. In contrast, in the downstream $[x/(c/\omega_{pi}) \gtrsim 1.5]$,

10

$\boldsymbol{u}_{i\perp}$ is nearly perpendicular to $\boldsymbol{E}_\perp$, but not completely perpendicular. We would like to stress that θ is nearly 90° and slightly less than 90°, and thereby ions collectively move also in the parallel direction to $\boldsymbol{E}_\perp$ and are energized by $\boldsymbol{E}_\perp$.
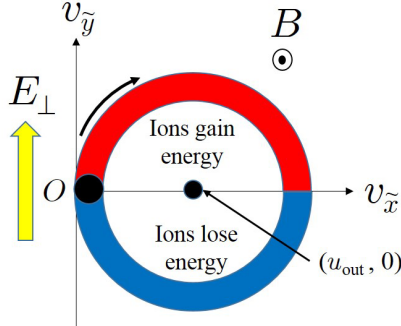

FIG. 6: Schematic diagram of the velocity distribution formed by nonadiabatic ions. The ions gain energy on the red semicircle and lose energy on the blue semicircle.

The ion bulk motion is oblique to $\boldsymbol{E}_\perp$, though each ion particle moves according to the $E_\perp \times B$ drift. This outcome can be consistently interpreted as follows. We show the schematic diagram of the velocity distribution structure formed by nonadiabatic ions in the velocity space of Fig. 6, where we employ the simplified geometry, i.e. the outflow $u_{\text{out}}{}^2$, the electric field $E_\perp$, and the magnetic field B are taken to be in the $\tilde{x}$, $\tilde{y}$, and $\tilde{z}$ directions, respectively The center of the circle is located at $(u_{\text{out}}, 0)$. A nonadiabatic ion rotates around $B_{\tilde{z}}$ moving in the $\tilde{x}$ direction owing to the $E \times B$ drift. In the velocity space shown in Fig. 6, an ion rotates clockwise on the circle according to the gyromotion. The gyromotion phase differs from particle to particle, and the difference of the gyromotion phase is likely to be based on the slight difference of the positions, times, and velocities at which ions enter the downstream and the fluctuations of the electromagnetic field. The ion fluid at a location is comprised of ion particles with various velocities owing to the mixture of ion particles with various gyromotion phases. In the velocity space, they are distributed on the circle. When ions are on the upper semicircle (the red curve), they are energized by $E_\perp$, whereas on the lower semicircle (the blue curve) they lose kinetic energy. If the ions are

---

[2] *To be exact, the below discussion demonstrates that the ion bulk motion changes to obtain the $\tilde{y}$-component through the heating process. However, we employ the initial outflow as u_{out}, assuming that the ion heating process does not work yet.*

B_{z0}/B_{x0}	0.5	1.0	2.0	3.0
$T_{i\perp}/(m_e c^2)$	0.093	0.071	0.042	0.038
u_{out}/c	0.020	0.021	0.029	0.031

TABLE I: Dependence of the ion perpendicular temperature and the outflow speed on the guide field strength. $T_{i\perp}$ tends to decrease and u_{out} has a tendency to become higher as B_{z0} is increased.

distributed uniformly on the circle, their energy gain is equal to the energy loss, and thus the total kinetic energy of the ions is not changed by $E_\perp$. However, the nonadiabatic ions enter the downstream with $v_\perp = \sqrt{v_{\tilde{x}}^2 + v_{\tilde{y}}^2}$ small enough compared with the outflow speed u_{out}. Therefore, the ions are initially located near the origin O and rotate clockwise on the circle. The ions pass along the red semicircle at first and then along the blue semicircle. This leads toward the understanding that the number of the ions on the upper semicircle is always larger than the number of ions on the lower semicircle, so long as nonadiabatic ions newly enter the downstream. Therefore, the collective motion of ions suffering this process is oblique to $E_\perp$, and the total energy of the ions is increased.

Figure 7 displays the ion velocity distributions shown in Fig. 3 in the $(v_{\tilde{x}}, v_{\tilde{y}})$ coordinate, where $v_{\tilde{x}} = \boldsymbol{v} \cdot (\boldsymbol{E}_\perp \times \boldsymbol{B})/(E_\perp B)$ and $v_{\tilde{y}} = \boldsymbol{v} \cdot \boldsymbol{E}_\perp/E_\perp$ $(v_{\tilde{z}} = \boldsymbol{v} \cdot \boldsymbol{B}/B)$. We can better understand how the ions gain kinetic energy through the effective heating process. It is more clearly seen at the boxed areas (B)-(D) in Fig. 2 that the number of ions with $v_{\tilde{y}} > 0$ (motion in the direction of $\boldsymbol{E}_\perp$) is larger than the number of ions with $v_{\tilde{y}} < 0$ (motion in the opposite direction of $\boldsymbol{E}_\perp$). Thus, it is confirmed that the bulk ion moves also in the direction parallel to $\boldsymbol{E}_\perp$, and ions gain kinetic energy from $\boldsymbol{E}_\perp$. In contrast, the structure shown in Fig. 7 (a) is apparently different from that in Fig. 3 (a), but it indicates that the ions at the boxed area (A) are mainly comprised of the magnetized particles which are not effectively heated yet and move in the $\tilde{x}$ direction according to the $E \times B$ drift.

C. Dependence on guide field strength

The effective heating of nonadiabatic ions are observed in cases of different strength B_{z0}. In Table 1, we summarize $T_{i\perp}$ and u_{out} observed for the cases of various B_{z0}/B_{x0}, where
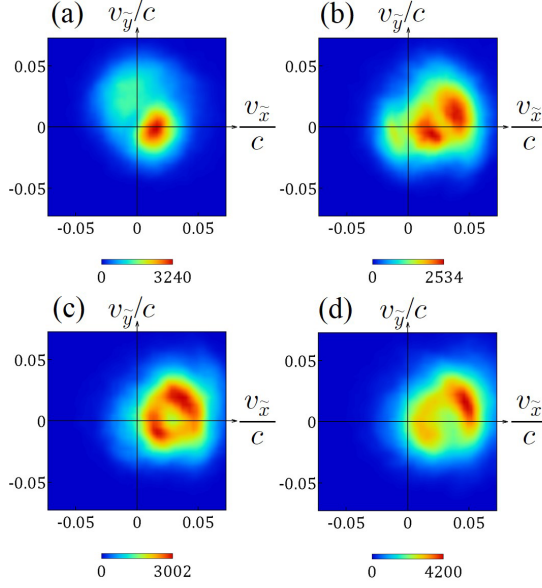
FIG. 7: Ion velocity distributions in the $(v_{\tilde{x}}, v_{\tilde{y}})$ coordinate, where $v_{\tilde{x}} = \boldsymbol{v} \cdot (\boldsymbol{E}_\perp \times \boldsymbol{B})/(E_\perp B)$ and $v_{\tilde{y}} = \boldsymbol{v} \cdot \boldsymbol{E}_\perp / E_\perp$.

the other parameters are the same as those in the case of $B_{z0}/B_{x0} = 2.0$ shown above. The ion temperature clearly tends to decrease as the guide field is increased, which is consistent with results reported by experiments [3, 15]. On the other hand, the effective heating process discussed in this paper is not sufficient to explain this tendency presented in Table 1, since the increment of the ion perpendicular temperature is theoretically estimated as $\Delta T_{i\perp} \simeq m_i u_{\text{out}}^2/2$. From Table 1, we can see that as the guide field becomes stronger, u_{out} becomes rather higher. This result theoretically leads to the opposite conclusion that $\Delta T_{i\perp}$ is larger as B_{z0} is higher.

This inconsistency between the theory and the simulation results implies that we must discuss the motions of nonadiabatic ions by taking account of finite v_y upon crossing the separatrix, which is regarded as zero in this work. If the initial v_y is finite, the radius of the circle formed by nonadiabatic ions is larger than that in the case of zero v_y. (In contrast, the initial positive finite v_x causes decrease in the radius of the circle.)

Moreover, another phenomenon also is responsible for this inconsistency. Crescent-like structures of ion velocity distributions are found in some cases. Figure 8 shows (a) the spatial profile of magnetic field lines and B_z/B_{x0}, and (b) and (c) ion velocity distributions in the case of $B_{z0}/B_{x0} = 3.0$. Figures 8 (b) and (c) correspond to the boxed areas (B) and

13

(C) of the panel (a), respectively. Comparing Figs. 8(b) and (c), we can see that the effective heating process surely works for ions, since the crescent-like structure rotates clockwise about the rotation center $(v_x, v_y) \sim (0.03, 0.0)c$, that is, ions move in the x direction rotating mainly around the guide field. Therefore, the formation of the crescent-like structure is due to essentially the same process as the formation of the ring-like structure. However, the crescent structure means that the ring is not completely formed. The incompletion of the ring shows that the effective heating has been suppressed due to a cause not yet identified, compared with the cases of the complete ring formation. If in the velocity space, we consider various sizes of the circular arc with the same radius, on which particles are distributed uniformly, the case of the complete circle clearly has the maximum standard deviation, that is, the maximum effective thermal velocity. That by what mechanism the incomplete ring structure (the circular arc), namely, the crescent-like structure, is formed in some cases will be discussed in the future paper.
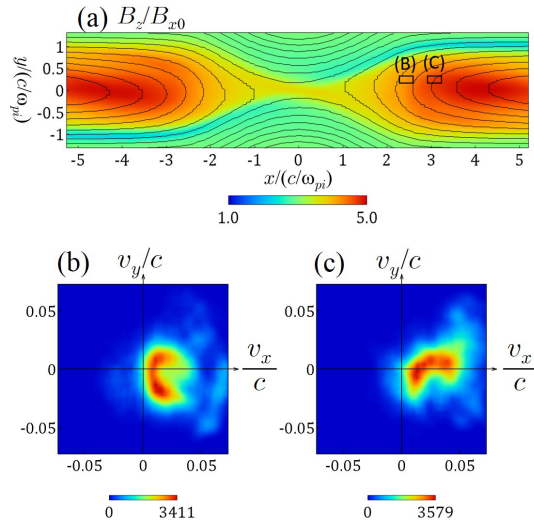

FIG. 8: Simulation results for the case of $B_{z0}/B_{x0} = 3.0$. (a) Spatial profile of magnetic field lines and B_z/B_{x0}. (b) Ion velocity distribution at the boxed area (B). (c) Ion velocity distribution at the boxed area (C). Crescent-like structures are formed.

14

IV.   COMPARISON WITH THE PICKUP

Finally, let us note that the behaviors of the nonadiabatic ions (protons as the main component ion) are similar to the "the pickup" of heavy ions.

The classic pickup, which was proposed by Möbius et al. in 1985, is the process in which if a neutral particle is newly ionized in the solar wind, the newly ionized particle behaves as nonadiabatic and is energized by the electromagnetic field [16]. In 2009, Drake et al. applied the classic pickup to magnetic reconnection in fully ionized plasmas [17–19]. Reviewing the theory of the pickup applied to magnetic reconnection, entering the downstream across the separatrix, the heavy ions, which are nonadiabatic, gain a convective velocity equal to the outflow velocity u_{out} and an effective thermal velocity u_{out}, and form a ring velocity distribution. The characteristic features of the velocity distribution in Fig. 3(c) fit well with features predicted by the pickup.

For the pickup, the following threshold has been calculated [18, 19].

$$\frac{m_i}{q_i} > \frac{10\sqrt{\beta_{x,\mathrm{up}}}}{\pi\sqrt{2}}\frac{m_p}{e},\tag{1}$$

where m_p and e are the mass and charge of the proton, m_i and q_i denote the mass and charge of the ion targeted for pickup, and $\beta_{x,\mathrm{up}} = 8\pi n(T_e + T_i)/B_{x,\mathrm{up}}^2$ is the ratio of the plasma pressure to the pressure of the antiparallel magnetic field in the upstream. Drake et al. also have argued that only ions with high mass-to-charge ratio (M/Q) to satisfy Eq. (1) can be treated as nonadiabatic and effectively heated by the pickup mechanism. In solar flares, where $\beta_{x,\mathrm{up}} > 1$, this mechanism can explain the enhanced abundance of energetic ions with high M/Q in flares. The relation Eq. (1), however, implies that the threshold M/Q is smaller as $\beta_{x,\mathrm{up}}$ is lower. We can point out that if $\beta_{x,\mathrm{up}} \ll 1$, which is satisfied in STs, the threshold M/Q becomes less than m_p/e, and thus protons can gain effective thermal velocities by suffering the pickup mechanism. Indeed, for the simulation of Fig.2-5, $\beta_{x,\mathrm{up}}$ is observed to be $\simeq 0.14$. By substituting this value of $\beta_{x,\mathrm{up}}$ into Eq. (1), we obtain as the pickup condition for our simulation, $m_i/q_i > 0.84 m_p/e$, which means that even proton can suffer the pickup.

However, it is necessary to note that Eq. (1) has been theoretically introduced under the following assumptions: the inflow speed is $0.1 v_{A\mathrm{up}}$ ($v_{A\mathrm{up}}$ is the Alfvén speed in the upstream), the separatrix thickness is nearly equal to the ion sound Larmor radius, and the guide field
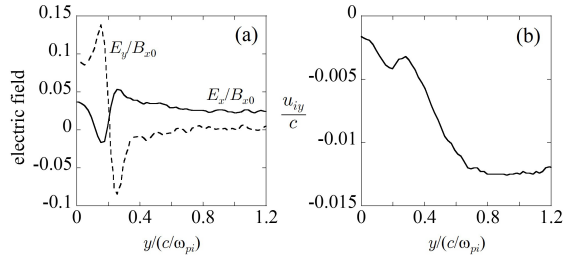
15

FIG. 9: (a) Electric field E_x (the solid line) and E_y (the dotted line) and (b) ion bulk velocity u_{iy} along the y-axis at $x/(c/\omega_{pi}) = 1.53$.

is extremely strong. Under these assumptions, Eq. (1) is equivalent to the relation that the period of time during which an ion passes across the separatrix is shorter than its gyroperiod. In cases of driven magnetic reconnection in our PASMO simulations, the above assumptions are not fully satisfied. For example, the guide field is taken to be $B_{z0}/B_{x0} = 0.5 - 3.0$, which is not extremely strong. Here, let us estimate the separatrix thickness and the plasma inflow speed in the case of our simulation and re-evaluate the nonadiabatic condition instead of Eq. (1). Figure 9 shows (a) the electric fields E_x and E_y, and (b) the y-component of the ion bulk velocity u_{iy} along the y-axis at $x/(c/\omega_{pi}) = 1.53$ in the case shown in Figs. 2-5. From Fig. 8(a), we can see that E_x (the solid line) and E_y (the dotted line) are sharply changed in the region between $y/(c/\omega_{pi}) \simeq 0.07$ and $y/(c/\omega_{pi}) \simeq 0.34$, from which we can estimate that the separatrix thickness is approximately $0.27/(c/\omega_{pi})$. Figure 9(b) indicates that the inflow speed is of the order of $0.005c$ at $y/(c/\omega_{pi}) \simeq 0.4$, which is the upstream close to the separatrix. Therefore, the period of time during which ions pass across the separatrix ΔT is obtained as $\omega_{pi}\Delta T \simeq 54$. On the other hand, the ion gyroperiod T_{ci} in the local magnetic field is given as $\omega_{pi}T_{ci} \simeq 110$. Thus, in the case of driven magnetic reconnection shown in Figs. 2-5, ions pass the separatrix for a shorter time than the gyroperiod, and ions can be fully regarded as nonadiabatic particles.

V. SUMMARY AND DISCUSSION

By means of electromagnetic particle simulations, we have studied the proton effective heating in the downstream of magnetic reconnection with a guide field. As shown by experimental results, the increment of the proton temperature has been found in the downstream

16

of magnetic reconnection. We also have observed a ring-like structure of the proton velocity distribution at a local point of the downstream. The characteristic features of the velocity distribution show that protons behave as nonadiabatic and are effectively heated according to the following process. Entering the downstream across the separatrix, the nonadiabatic protons suddenly feel the electromagnetic field. The entry speed of such protons is much smaller than the outflow speed. In the downstream, *each proton particle rotates mainly around the guide magnetic field with $E_\perp \times B$ drifting ($E_\perp$ is the electric field perpendicular to the magnetic field), but the protons collectively moves obliquely to $E_\perp$ and gain energy from $E_\perp$. It is because that the number of protons moving in the direction of $E_\perp$ is larger than the number of protons moving in the opposite direction of $E_\perp$.*

This effective heating mechanism for nonadiabatic protons is similar to the pickup applied to magnetic reconnection. The pickup was thought to be responsible for only heavy ions above the theoretical threshold of mass-to-charge as minor ion components. In this work, however, we have demonstrated that even if the effective heating process of protons is interpreted as the pickup, the interpretation does not include inconsistency with the known pickup in the cases that plasma beta is quite low in the upstream as STs.

Furthermore, it should be noted that in laboratory as well as in space and astrophysical plasmas, multiple X-points are present, since, for instance the plasmoid instability arises [20, 21] and intermittent reconnection is driven [10, 22]. This implies that protons suffer the effective heating mechanism reported by this work every time the protons go through the downstream of an X-point. As a result, the effective heating may work many times for protons to potentially allow quite high heating of protons.

---

[1] M. Gryaznevich, R. Akers, P. G. Carolan, N. J. Conway, D. Gates, A. R. Field, T. C. Hender, I. Jenkins, R. Martin, M. P. S. Nightingale, C. Ribeiro, D. C. Robinson, A. Sykes, M. Tournianski, M. Valovič, and M. J. Walsh, Phys. Rev. Lett. **80**, 3972 (1998).

[2] M. Yamada, R. Kulsrud, and H. Ji, Rev. Mod. Phys. **82**, 603 (2010).

[3] Y. Ono, H. Tanabe, Y. Hayashi, T. Ii, Y. Narushima, T. Yamada, M. Inomoto, and C. Z. Cheng, Phys. Rev. Lett. **107**, 185001 (2011).

[4] Y. Ono, H. Tanabe, T. Yamada, M. Inomoto, T. Ii, S. Inoue, K. Gi, T. Watanabe, M. Gryaznevich, R. Scannell, C. Michael, and C. Z. Cheng, Plasma Phys. Control. Fusion **54**, 124039 (2012).

[5] J. Yoo, M. Yamada, H. Ji, J. Jara-Almonte, and C. E. Myers, Phys. Plasmas **21**, 055706 (2014).

[6] N. F. Loureiro, A. A. Schekochihin, and A. Zocco, Phys. Rev. Lett. **111**, 025002 (2013).

[7] R. Numata and N. F. Loureiro, J. Plasma Phys. **81**, 305810201 (2014).

[8] R. Horiuchi and T. Sato, Phys. Plasmas **4**, 277 (1997).

[9] W. Pei, R. Horiuchi, and T. Sato, Phys. Rev. Lett. **87**, 235003 (2001).

[10] W. Pei, R. Horiuchi, and T. Sato, Phys. Plasmas **8**, 3251 (2001).

[11] S. Inoue, Y. Ono, H. Tanabe, R. Horiuchi, and C. Z. Cheng, Nucl. Fusion **55**, 083014 (2015).

[12] H. Ohtani and R.Horiuchi, Plasma Fusion Res. **4**, 024 (2009).

[13] R. Horiuchi, S. Usami, and H. Ohtani, Plasma Fusion Res. **9**, 1401092 (2014).

[14] R. Horiuchi and H. Ohtani, Comm. Comput. Phys. **4**, 496 (2008).

[15] Y. Ono, Y. Hayashi, T. Ii, H. Tanabe, S. Ito, A. Kuwahata, T. Ito, Y. Kamino, T. Yamada, M. Inomoto, and TS-Group, Phys. Plasmas **18**, 112113 (2011).

[16] E. Möbius, D. Hovestadt, B. Klecker, M. Scholer, G. Gloeckler, and f. M. Ipavich, Nature **318**, 426 (1985).

[17] J. F. Drake, M. Swisdak, T. D. Phan, P. A. Cassak, M. A. Shay, S. T. Lepri, R. P. Lin, E.

Quataert, and T. H. Zurbuchen, J. Geophys. Res. **114**, A05111 (2009).

[18] J. F. Drake, P. A. Cassak, M. A. Shay, M. Swisdak, and E. Quataert, Astrophys. J. **700**, L16 (2009).

[19] J. F. Drake and M. Swisdak, Phys. Plasmas **21**, 072903 (2014).

[20] L. Comisso, M. Lingam, Y.-M. Huang, and A. Bhattacharjee, Phys. Plasmas **23**, 100702 (2016).

[21] F. Pucci and M. Velli, Astrophys. J. Lett. **780**, L19 (2014).

[22] S. Usami, R. Horiuchi, H. Ohtani, and M. Den, J. Phys. Conf. Ser. **561**, 012021 (2014).